Relevance of Chemical vs. Electrochemical Oxidation of Tunable Carbene Iridium Complexes for Catalytic Water Oxidation

Olivares, M.; Ham, C.J.M. van der; Mdluli, V.; Schmidtendorf, M.; Müller-Bunz, H.; Verhoeven, T.W.G.M.; ... ; Albrecht, M.

ChemPubSoc Europe

DOI: 10.1002/ejic.202000090

EurJIC European Journal of Inorganic Chemistry

Full Paper

Water Oxidation

Relevance of Chemical vs. Electrochemical Oxidation of Tunable Carbene Iridium Complexes for Catalytic Water Oxidation

Marta Olivares,[a,b] Cornelis J. M. van der Ham,[c] Velabo Mdluli,[d] Markus Schmidtendorf,[b] Helge Müller-Bunz,[b] Tiny W. G. M. Verhoeven,[e] Mo Li,[d] J. W. (Hans) Niemantsverdriet,[f] Dennis G. H. Hetterscheid,*[c] Stefan Bernhard,*[d] and Martin Albrecht*[a,b]

Abstract: Based on previous work that identified iridium(III) Cp* complexes containing a *C,N*-bidentate chelating triazolylidene-pyridyl ligand (Cp* = pentamethylcyclopentadienyl, $C_5Me_5^-$) as efficient molecular water oxidation catalysts, a series of new complexes based on this motif has been designed and synthesized in order to improve catalytic activity. Modifications include specifically the introduction of electron-donating substituents into the pyridyl unit of the chelating ligand (H, **a**; 5-OMe, **b**; 4-OMe, **c**; 4-*t*Bu, **d**; 4-NMe_2, **e**), as well as electronically active substituents on the triazolylidene C4 position (H, **8**; COOEt, **9**; OEt, **10**; OH, **11**; COOH, **12**). Chemical oxidation using cerium ammonium nitrate (CAN) indicates a clear structure-activity relationship with electron-donating groups enhancing catalytic turnover frequency, especially when the donor substituent is positioned on the triazolylidene ligand fragment (TOF_{max} = 2500 h^{-1} for complex **10** with a MeO group on pyr and a OEt-substituted triazolylidene, compared to 700 h^{-1} for the parent benchmark complex without substituents). Electrochemical water oxidation does not follow the same trend, and reveals that complex **8b** without a substituent on the triazolylidene fragment outperforms complex **10** by a factor of 5, while in CAN-mediated chemical water oxidation, complex **10** is twice more active than **8b**. This discrepancy in catalytic activity is remarkable and indicates that caution is needed when benchmarking iridium water oxidation catalysts with chemical oxidants, especially when considering that application in a potential device will most likely involve electrocatalytic water oxidation.

Introduction

Water splitting has been considered as the key chemical technology to store transient energy from renewable sources such as wind and sunlight and is therefore critical for reducing our dependence on slow-growing fossil feedstocks.[1–4] While the water reduction half-cycle providing H_2 as high-energy fuel has been investigated with considerable success,[5–8] the water oxidation half-cycle is much more challenging due to the harsh conditions and the molecular complexity of O_2 formation from H_2O oxidation.[9–11] As a consequence, much effort has been devoted to the development of catalysts that mediate water oxidation, including semiconductor materials as well as molecularly defined metal complexes. Amongst the various classes of homogeneous catalysts, ruthenium(II)[12,13] and iridium(III)[14,15] complexes have shown particularly promising properties,[16–21] the former through remarkably high turnover frequencies,[22] the latter by their exceptional longevity with turnover numbers of tens of thousands.[23] Despite the harsh conditions required for water oxidation, it has been demonstrated that iridium(III) Cp* complexes remain efficient homogeneous catalysts, provided they contain a chelating ligand.[24–28] This behavior enabled mechanistic investigations, which revealed (i) that the Cp* ligand is degraded, presumably during catalyst activation,[29–33] and (ii) that bidentate chelating ligands containing strong donors such as alkoxides or (abnormal) carbenes enhance catalytic activity,[26,34–37] suggesting involvement of a high-valent iridium species in the turnover-limiting step. Mechanistic investigations of homogeneous water oxidation catalysis with molecular sacrificial oxidant such as oxone ($KHSO_5$), $NaIO_4$, or cerium ammonium nitrate {CAN, $(NH_4)_2[Ce(NO_3)_6]$} unveiled a prominent role of the sacrificial oxidation,[38] and catalyst performance varies considerably when modulating the terminal oxidant from e.g. $NaIO_4$ to CAN.[39,40] This variation has been attributed in parts to the fact that some oxidants such as oxone or $NaIO_4$ are also oxygen donors,[38] and in other parts to direct interactions between the metal center and the oxidant,[41,42] which limits the usefulness of the oxidant as a proxy to short-cut the water reduction cycle.

[a] *Departement für Chemie und Biochemie, Universität Bern, Freiestrasse 3, CH-3012 Bern, Switzerland*
E-mail: martin.albrecht@dcb.unibe.ch
bern@cmu.edu
[b] *School of Chemistry, University College Dublin, Belfield, Dublin 4, Ireland*
[c] *Leiden Institute of Chemistry, Leiden University, 2300 RA, Leiden, The Netherlands*
d.g.h.hetterscheid@chem.leidenuniv.nl
[d] *Department of Chemistry, Carnegie Mellon University, Pittsburgh, Pennsylvania 15213, USA*
[e] *Department of Chemical Engineering and Chemistry, Eindhoven University of Technology, P.O. Box 513, 5600 MB Eindhoven, The Netherlands*
[f] *SynCat@DIFFER, Syngaschem BV, P.O. Box 6336, 5600 HH Eindhoven, The Netherlands*
Supporting information and ORCID(s) from the author(s) for this article are available on the WWW under https://doi.org/10.1002/ejic.202000090.

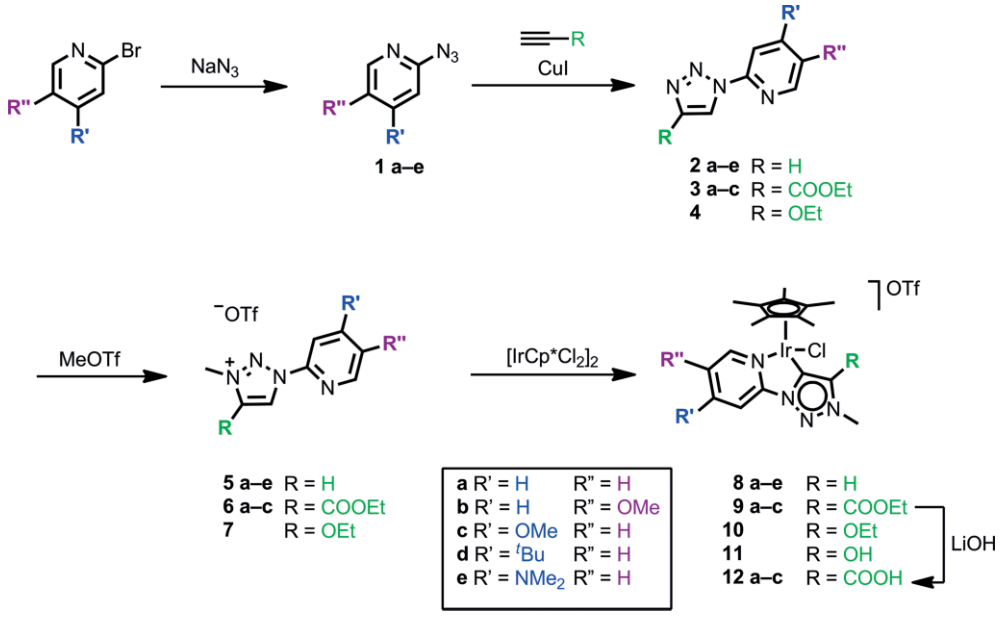

Scheme 1. Synthesis of the triazolium salts (**5a–e**, **6a–c**, **7**) and iridium complexes (**8a–e**, **9a–c**, **10**, **11** and **12**).

In an actual water splitting device, the hole injection into the water oxidation catalyst will be coupled with electron injection to the water reduction catalyst in a closed loop. Such charge separation is most conveniently imparted by a (photo)electrode, and therefore, catalyst performance under electrochemical oxidation will be essential.[43] When considering the distinct role established for various sacrificial oxidants, it seems unclear whether the catalytic activity of a given catalyst in the presence of a molecular oxidant is correlated to water oxidation activity under electrochemical conditions. We have therefore engaged in optimizing iridium complexes containing a *N,C*-bidentate chelating pyridyl-triazolylidene ligand as a lead structural motif, which have demonstrated previously outstanding molecular integrity under acidic conditions as well as excellent turnover numbers for CAN-mediated water oxidation.[26,27] Here we show that ligand modifications at both the pyridyl and the carbenic[44–47] triazolylidene site allows the catalytic activity of the iridium center to be rationally tailored for CAN-driven water oxidation. However, the catalytic performance mediated by this sacrificial oxidation does not correlate with the performance in electrochemical water oxidation and distinctly different orders of activity have been established. This divergence suggests that caution is needed when benchmarking iridium catalysts by chemical oxidants for water oxidation catalysis. This conclusion is supported by a previous study on manganese oxides for water oxidation.[48] and complements related work on the Crabtree–Brudvig Ir(pyalk) system.[49]

Results and Discussion

1. Synthesis and Characterization of a Series of Pyridyl-Triazolylidene Iridium Complexes with Different Substitution Patterns

Functionalization of the pyridyl-carbene ligand on both the carbene and the pyridyl units was facilitated by the functional group tolerance of the [3+2] cycloaddition of alkynes and azides,[50–52] and the commercial availability of various alkynes and substituted 2-bromopyridines. These bromopyridines were readily converted into the pyridyl azides **1** via a copper-catalyzed substitution with NaN_3 (Scheme 1). Subsequent copper-catalyzed "click" cycloaddition formed the triazoles **2**–**4**, which were alkylated selectively at the N3 position in high yields by using MeOTf, thus affording the pyridyl-triazolium salts **5**–**7** as carbene ligand precursors.[53–58] A variety of functional groups were incorporated to probe their effect on catalytic water oxidation. Specifically, different electron donating groups were installed onto the pyridyl ring in order to stabilize the critical high-valent iridium transition states,[33] including –OMe, –*t*Bu or $–NMe_2$ groups in 4-position, and a –OMe group in 5-position (**5b**–**e**). The triazole heterocycle was modulated by incorporating a –COOEt group at C4 position as a functional group (**6a**–**c**), which after hydrolysis has the potential to engage in reversible (de)protonation to facilitate electron-coupled proton transfer processes.[59–61] The ester functionality offers a reference to distinguish electronic withdrawing properties of the carboxylate group from proton shuttling effects of the –COOH unit, which are blocked with the ester unit. Complementary, an alkoxy substituent was introduced at the triazole (**7**) as a functional group that serves as electron donor and potential hydrogen-bond acceptor,[62] and after dealkylation, as proton shuttle.[63,64] These modifications gave access to a range of ligands with different electronic properties, demonstrating the flexibility of triazole-derived carbene precursors.

Metalation of the triazolium salts **5**–**7** was accomplished upon reaction with $[IrCp^*Cl_2]_2$ in toluene at elevated temperatures in the absence of a base. These conditions induced triazolium C–H bond activation via cyclometalation and afforded the mesoionic carbene complexes **8**–**11** as yellow solids that precipitated from the reaction solution. While all complexes formed within 1–2 days, complex **9b** with an ester functionality

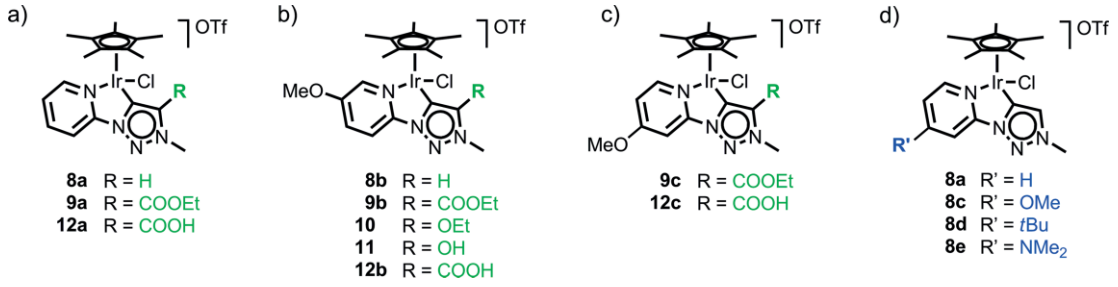

Figure 1. Complexes with a) unfunctionalized pyridyl and different groups on the triazolylidene, b) with 5-OMe pyridyl and functionalized triazolylidene, c) with 4-OMe pyridyl and functionalized triazolylidene, and d) with unfunctionalized triazolylidene and variable substituents at the pyridyl *para* position.

and –OMe substituent in the pyridyl 5-position reacted much slower and required 6 days. The absence of any additives for the metalation is advantageous in the presence of functional groups on the ligands, as for example strong bases would induce ester cleavage. However, we noted that the formation of complex **10** with an ethoxy-substituent on the triazolylidene was accompanied by partial ether hydrolysis, affording complex **11** with an –OH substituent on the triazolylidene as a minor product (approximately 10 %). Complex **11** is the first N-heterocyclic carbene with a hydroxide adjacent to the carbenic carbon, a design that is not conceivable for example in imidazolium-derived Arduengo carbenes due to the lability of the N–O bond. Furthermore, complexes **12a**–**c** with a pendant carboxylic acid unit were obtained by ester hydrolysis from the corresponding complexes **9a**–**c** using methanolic LiOH (Scheme 1). All complexes **8**–**12** were completely air and moisture stable and were purified via standard column chromatography over silica in moderate to high yield.

NMR Characterization. All complexes were fully analysed by ^{1}H and ^{13}C NMR spectroscopy and showed the expected pyridyl and triazolylidene signal patterns. To compare the effect of the donor groups on the triazolylidene and on the pyridyl ligand, it is instructive to compare series of complexes that are comprised of an identical substitution pattern on one of the two heterocycles while the functionality on the other heterocycle is varied. For example, the series of complexes **8b**, **9b**, **10**, **11**, and **12b** all feature the same 5-methoxy-substituted pyridyl unit, but different substituents on the triazole heterocycle, and the series of complexes **8a**, **8c**–**e** all feature the same triazolylidene ring, but different functional groups on the 4-substituted pyridyl unit (Figure 1).

Modification of the substituent R on the triazolylidene unit has an obvious effect on the electronic configuration of the carbene heterocycle as inferred from the gradual shift of the NCH_3 resonance from low field (δ_H = 4.56 for R = COOH, COOEt) continuously to higher field for the unsubstituted complex **8b** (δ_H = 4.45 for R = H) and even more pronounced for electron-donating substituents in **10** and **11** (δ_H = 4.20 for R = OEt, OH). No such correlation was observed for the proton resonances attributed to the pyridyl and Cp* units. The ^{13}C NMR chemical shift of the metal-bound carbenic resonance appears at rather high field with the OH/OEt substituents (δ_C = 138) compared to the unsubstituted and carboxylate-functionalized derivatives (δ_C = 153 for **8b** and **12b**). The ester group induced the most deshielded resonance in this series (δ_C = 158 for **9b**). While the NCH_3 group provides an useful probe for inductive effects, the ^{13}C NMR resonance shifts obviously combine mesomeric and inductive effects. The absence of any clear correlation between electronic properties of the substituents and resonance frequencies of the carbenic carbon illustrate the difficulties in using ^{13}C NMR shifts to correlate electronic properties of N-heterocyclic carbenes.[65,66]

Similarly, modification of the pyridyl substituent R' had only very limited effects on the adjacent heterocycle. Variation of R' from H to *t*Bu, OMe, and NMe_2 resulted in a small shift of the triazolylidene C4-bound proton resonance (δ_H = 8.16 for **8a** vs. 8.17, 8.15, and 8.07 for **8c**–**e**, all in CD_3CN), which correlates reasonably with the Hammett parameter of the donor group (σ_{meta} = +0.12 for OMe, –0.10 for *t*Bu, and –0.16 for NMe_2).[67] with the increasing donor properties of R'. The carbenic resonance is not affected and appears for all complexes **8c**–**e** at 157 ppm. Local effects are obviously stronger on the pyridine ring itself, resulting in shift differences between **8a** and **8e** of more than 1 ppm.

Structural Characterization in the Solid State. The solid-state structures of complexes **8**–**12** were determined by single-crystal X-ray diffraction analyses and confirmed the connectivity pattern deduced from NMR spectroscopy. All complexes show the typical three-legged piano-stool geometry around the iridium center as expected for this type of half-sandwich iridium complexes.[68–70] Representative molecular structures of complexes **8b**, **9a**–**b** and **10** are shown in Figure 2 (see Supporting Information for the structures of complexes **8d**, **8e**, **9c**, **11**, **12a**, and **12b**). Selected bond lengths and angles are listed in Table 1. Bond lengths and angles around the iridium center are unsurprising for complexes **8b**, **9a**–**b** (Table 1) and also for all structures reported in the supporting information, revealing no significant differences to reported triazolylidene iridium(III) complexes.[68–70] In contrast, the bonding in complex **10** deviates considerably. In particular the carbene–iridium bond is unusually long [Ir–C_{trz} = 2.19(1) Å, *cf* 2.02(1) Å in the other complexes]. This large distance is counterbalanced by much shorter bonds to all the other ligands, in particular to the chloride [Ir–Cl = 2.27(1) Å in **10** vs. 2.40(1) Å usually observed], and to the Cp* ligand, which is about 0.1 Å closer [Ir–Cp_{centr} = 1.72(1) vs. averaged 1.82(1) Å]. Furthermore, it is worth noting that the C_{trz}–C_{trz} bond in complex **10** is remarkably long, 1.480(1) Å, indicative of a single bond rather than the typically observed 1.37–1.39 Å for this formally conjugated bond. While the C_{trz}–O_{OEt} distance of 1.34(1) Å is similar to other aryl–O bonds [e.g.

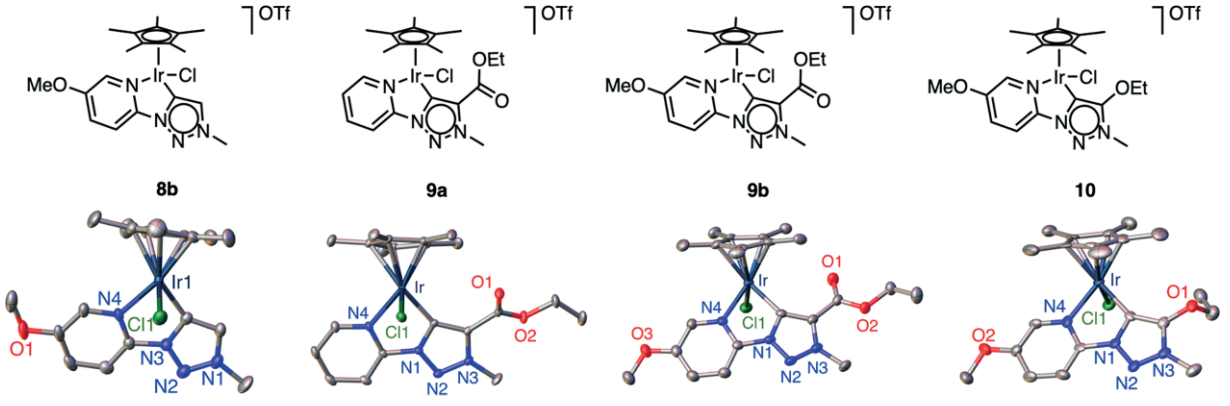

Figure 2. Schematic drawing and ORTEP plots for complexes **8b**, **9a**, **9b** and **10** (50 % probability, H atoms, non-coordinating anions, co-crystallized solvent molecules, and second independent molecule of **10** omitted for clarity).

1.35(1) Å in complexes **8b** and **9b**], the pyridyl C–OMe bond is considerably stretched with 1.45(1) Å. Even though the bonding parameters of complex **10** deviate considerably from average, we note that complex **11** with an –OH substituent does not show similar behavior and the bond lengths and angles are commensurate to the metrics typically observed in such iridium complexes. Therefore, the deviations cannot be attributed to the presence of the oxo substituent but may be a curiosity, possibly induced by packing effects.[69]

Table 1. Selected bond lengths [Å] and angles [°] for complexes **8b**, **9a**, **9b** and **10**.

	8b	9a	9b	10[a]
Ir–N_{py}	2.123(4)	2.1204(15)	2.123(3)	2.091(8)
Ir–C_{trz}	2.026(5)	2.0198(17)	2.025(4)	2.185(9)
Ir–Cp*(cent)	1.802(3)	1.811(1)	1.818(1)	1.725(4)
Ir–Cl	2.4092(13)	2.4094(4)	2.3959(4)	2.275(2)
C_{trz}–C_{trz}	1.377(7)	1.391(2)	1.383(5)	1.480(13)
C_{trz}–Ir–N_{py}	76.67(18)	77.25(6)	77.41(14)	78.0(4)

[a] Bond lengths [Å] and angles [°] for second independent complex molecules in the unit cell are identical within esds.

2. Chemical Water Oxidation Using Cerium(IV) as Sacrificial Oxidant

We investigated the performance of these functionalized carbene iridium complexes in water oxidation catalysis, firstly chemically driven by using cerium ammonium nitrate (CAN) as sacrificial oxidant.[38] Reactions were run initially at a 7,200:1 CAN/iridium ratio (0.37 M CAN) and were quantified by manometry and GC-MS.[71] All complexes **8**–**12** showed appreciable activity and high robustness under these conditions, reaching the theoretical limit of oxygen production within about 5 h (Figure 3a). However, a closer inspection reveals distinct trends in activity.

The addition of different electron donating groups (–NMe_2, –*t*Bu, –OMe) either at C(4) or C(5) position of the pyridyl unit consistently enhanced the catalytic activity of the complexes compared to the ones bearing unmodified pyridine (entry 1 vs. 2–5; entry 6 vs. 8, 9; entry 11 vs. 12; Table 2, Figure 3b). The effect is considerable, for example complex **9b** with a –OMe group at the pyridyl C(5) has a 3-fold higher turnover frequency

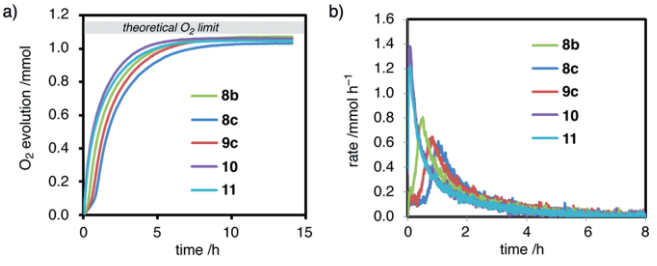

Figure 3. a) Oxygen evolution traces for complexes **8b**, **8c**, **9c**, **10** and **11** as representative complexes of the series; b) and time-dependent variation of oxygen evolution rates (right).

than the parent complex **9a** (TOF_{max} 1200 vs. 390 h^{-1}, entry 6 vs. 7). These substitution changes afford TOFs as high as 1500 h^{-1} for complex **8b** containing a OMe group *meta* to the iridium-bound pyridyl nitrogen.

Table 2. Catalytic water oxidation with iridium complexes **8**–**12**.[a]

Entry	Complex	R′ (pyr)	R (trz)	Conc [μM]	TON	TOF_{max} [h^{-1}]
1	**8a**	H	H	50.1	1920	700
2	**8b**	5-OMe	H	49.2	1980	1500
3	**8c**	4-OMe	H	50.9	1850	800
4	**8d**	4-*t*Bu	H	49.1	1860	540
5	**8e**	4-NMe_2	H	50.8	1850	1200
6	**9a**	H	COOEt	49.7	1800	390
7	**9b**	5-OMe	COOEt	49.3	1900	1200
8	**9c**	4-OMe	COOEt	50.1	1840	460
9	**10**	5-OMe	OEt	50.3	1920	2500
10	**11**	5-OMe	OH	49.8	1920	2200
11	**12a**	H	COOH	49.9	1740	230
12	**12c**	4-OMe	COOH	49.5	1780	350

[a] Reaction medium: 0.37 M CAN in 10 mL of 1 M HNO_3 (max O_2 = 1.0 mmol).

Modification of the triazolylidene substituents reveals that –COOEt, –COOH groups consistently decrease catalytic activity (entry 1 vs. 6, 11), with complex **9a** containing a COOEt group performing slightly better than complex **12a** with a COOH substituent (TOF_{max} = 390 vs. 230 h^{-1}, compare 700 h^{-1} for benchmark complex **8a**). A similar ca. 100 h^{-1} difference in TOF_{max} was also observed when the pyridine was modified with a methoxy group (entry 8 vs. 12), although the incorporation of the OMe group increased the overall activity compared to the

unfunctionalized pyridine complexes. These results demonstrate that the COOH group on the triazole heterocycle does not impart any beneficial proton shuttling function that might enhance the catalytic activity of these complexes, presumably because the highly acidic reaction conditions prevent (reversible) deprotonation of this benzoic acid-like COOH group. Instead, the electron-withdrawing character of this group prevails and leads to a decrease in catalytic water oxidation activity. In agreement with this predominantly electronic role of the triazolylidene substituent, the introduction of an electron-donating –OEt or –OH substituents enhanced the catalytic activity substantially, reaching turnover frequencies of 2500 and 2200 h^{-1} (entries 9, 10). This is a substantial increase compared to the TOF_{max} of 1500 h^{-1} for the corresponding complex **8b** with an unsubstituted triazolylidene unit (entry 2). These rates are higher than that of most iridium-based water oxidation catalysts which typical range from 700–1500 h^{-1}, though less active than the fastest known iridium-based catalysts (TOF_{max} 6,000–10,000 h^{-1}).[37,39] Most notably, however, the activity of these pyridyl-triazolylidene iridium complexes is rationally tunable by modulating the donor properties of both the pyridyl and the triazolylidene ligand units, indicative of a catalytically active species that comprises the pyridyl-triazolylidene ligand bound to the iridium center. Moreover, the correlation of turnover frequencies with ligand donor properties strongly suggests a turnover-limiting step that involves the build-up of positive charge, e.g. strongly donating ligands facilitate the accessibility of a high-valent iridium species such as an iridium(V)=O complex or an iridium(IV)–oxyl species as critical intermediates en route to O–O bond formation.

Monitoring the oxygen evolution rates over time reveals minor induction times for some of the iridium complexes. Variable activity in the low turnover regime is demonstrated when plotting the initial 15 min of water oxidation (Figure 4) for selected complexes **8**–**10**. This selection includes benchmark compound **8a** without any functionality, **9a** as relatively low-performing catalyst due to the electron-withdrawing substituent on the triazole, complexes **8b** and **9b** which contain an electron-donating pyridyl substituent imparting intermediate activity, as well as complex **10** with two electron-donating substituents and revealing the highest activity in this series.

The initial activity reflects some of the long-term trend reasonably well. Complex **10** shows essentially no induction period and assumes highest activity of the series immediately with induction times of a few seconds at best. Complex **8b** is turning over slightly better than the other complexes of this set with noticeable O_2 evolution starting after about 180 seconds (Figure 4). In contrast, complexes **8a** and **9a**–**b** show only poor activity in this early time regime, in agreement with the low initial TOF noted earlier (cf. Figure 3b). The very low turnovers observed for these complexes in the first 15 min (TOF < 10 h^{-1}) suggest that catalyst activation is relatively slow for these complexes (e.g. TOF_{max} of **9b** = 1200 h^{-1}).

3. Electrochemical Water Oxidation

Water oxidation was expanded towards electrochemical water oxidation catalysis. Based on CAN results, a specific set of complexes was chosen for these experiments including complex **9a** as relatively low-performing catalyst due to the electron-withdrawing substituent on the triazole, complexes **8b**, and **9b** which contain an electron-donating substituent and show intermediate activity, and complex **10** with two electron-donating substituents and revealing highest activity in this series with a TOF_{max} that is about 6 times higher than that of **9a** (*cf* Table 1). In order to facilitate comparison, all electrochemical experiments were carried out at the same temperature and pH as applied in CAN-driven water oxidation.

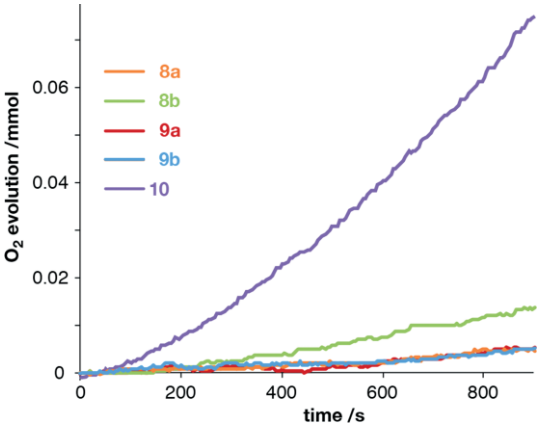

Figure 4. Oxygen evolution traces for the initial 15 min of chemical water oxidation for complex **8a**, **8b**, **9a**, **9b**, and **10**, indicating an enhanced activity of **8b**, and considerably enhanced activity of **10** at initial reaction times.

Figure 5 shows the cyclic voltammetry measurements for 0.5 mM solutions of complexes **8b**, **9a**, **9b** and **10** at an ITO electrode. Experiments using a gold electrode gave identical results, indicating no major role of the nature of the electrode. All complexes gave rise to a catalytic current that started at around 1.8 V vs. RHE. The similar behavior of complexes **9a** and **9b** suggests that modifications on the pyridine ring does not have a direct effect on the catalytic activity in electrochemical water oxidation. Complex **8b** showed by far the highest catalytic current followed by **9a** and **9b** and **10** shows the least catalytic activity. The catalytic activity of the catalysts, and in particular in case of complex **8b**, increased significantly over time.

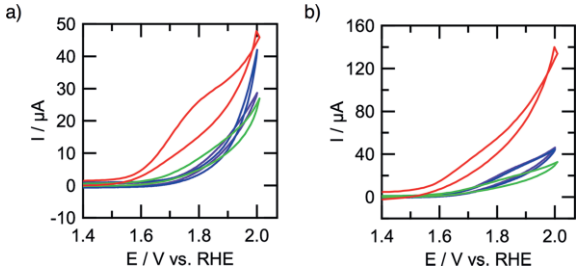

Figure 5. Overlaid CV plots of 0.5 mM solutions of **8b** (red), **9a** (purple), **9b** (blue), and **10** (green) in 0.1 M $HClO_4$, ν = 100 mV s^{-1} at an ITO working electrode (0.35 cm^2). Shown are the voltammograms of the fifth scan (a) and the 100th scan (b).

More detailed insights of catalytic water oxidation were obtained by chronoamperometry (CA) measurements with complexes **8b**, **9a**, **9b** and **10** (Figure 6). When a potential of 1.7 V

vs. RHE was continuously applied (Figure 6a), all complexes showed a similar behavior with almost no O_2 produced, as concluded from the low current throughout the experiment. In contrast, upon application of a 1.8 V vs. RHE (Figure 6b), the current density increased substantially, in particular with complex **8b**. The current increases gradually during the first 400 s after potential onset and reaches a plateau at about 120 μA, which is almost 10 times larger than the 12–14 μA current achieved by the other complexes of that series under identical conditions. Complex **10** displays a marginally higher activity initially compared to **9a** and **9b**, but this minor difference levels completely out after about 600 s, indicating similar electrocatalytic activity of these three samples.

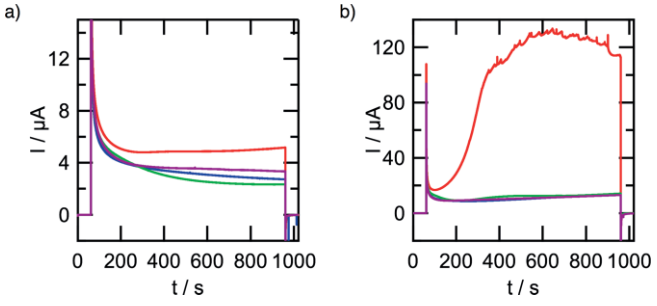

Figure 6. Chronoamperometry of 0.5 mM solutions of **8b** (red), **9a** (purple), **9b** (blue) and **10** (green) in 0.1 M $HClO_4$; a): A potential of 0.7 V was applied for 60 seconds, followed by 1.7 V for 900 seconds and 0.7 V for 60 seconds; b): A potential of 0.7 V was applied for 60 seconds, followed by 1.8 V for 900 seconds and 0.7 V for 60 seconds.

The trend in activity observed for complexes **8b**, **9a**, **9b** and **10** recorded by CA agrees well with the corresponding CV traces (*cf* Figure 5). The CA experiments clearly show that the catalysts are activated rapidly when a potential of at least 1.8 V vs. RHE is applied, while currents are mediocre at 1.7 V vs. RHE. From Figure 5, an onset potential of slightly less than 1.6 V vs. RHE is deduced. The activity trend extracted from these electrochemical water oxidation measurements is **8b** >> **9a** ≈ **9b** ≈ **10**, with **8b** about one order of magnitude more active than the other three complexes. Interestingly, this trend is considerably different from that determined by CAN-mediated chemical water oxidation, which reveals an activity decrease along the series **10** > **8b** ≈ **9b** > **9a** for TOF_{max}, and **10** > **8b** > **9a** ≈ **9b** for the initial TOF during the first 15 min, i.e. the time frame of the electrochemical experiments. This discrepancy strongly suggests diverging activation pathways and different active species in CAN-driven and electrochemical water oxidation. Because of their digressing behavior under different water oxidation conditions, complexes **8b** and **10** as the most active complexes in electrochemical and CAN-mediated water oxidation, respectively, were further investigated by electrochemical quartz crystal microbalance (EQCM) and online electrochemical mass spectrometry (OLEMS) measurements.

Electrochemical Quartz Crystal Microbalance (EQCM) Measurements. Measurements using an EQCM allows to detect any changes on the electrode surface resulting e.g. from deposition of a heterogeneous active layer on the electrode,[72–74] and has been successfully applied for investigating water oxidation catalysts.[24,43,75] In contrast to all other electrochemical experiments, the electrode is not in a hanging meniscus configuration, but mounted at the bottom of the EQCM cell. As a consequence of this set-up, the electrode surface is about 7 times larger (0.35 cm^2) than the electrode used in classical electrochemical experiments. The positioning of the electrode on the bottom of the cell increases the sensitivity for potential material deposition on the electrode due to gravity, whereas the larger electrode size affects diffusion patterns around the electrode.

Cyclic voltammetry of complex **8b** with an EQCM as electrode confirmed the constant current increases over time with a concerted shift of the onset potential to about 1.55 V vs. RHE (Figure 7). The frequency of the EQCM signal increases steadily with increasing numbers of cycles, which would correspond to a decrease in mass of the electrode. A more reasonable explanation is that the hydrophobicity of the local environment of the working electrode increases due to the evolution of dioxygen, which results in a positive frequency shift of the QCM signal. While these measurements do not rigorously rule out some material deposition, it is worth noting the different behavior of complex **10** under identical conditions. Repetitive potential cycling does not result in a significant increase of current and hence catalytic activity, yet deposition of material on the electrode surface is clearly demonstrated by a considerable decrease of the QCM frequency. Deposition does, however, not result in an active layer, since also after several cycles, the onset current density around 1.6 V does not increases and is far lower than that of complex **8b**. These experiments suggest formation of an active homogeneous species with complex **8b** under electrochemical conditions, while complex **10** forms an inactive heterogeneous layer. This heterogeneous deactivation may rationalize the lower current density observed with complex **10** in chronoamperometry and contrasts the high activity of complex **10** in CAN-mediated water oxidation.

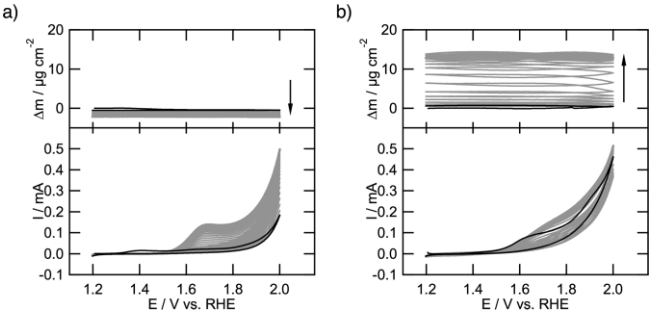

Figure 7. Calculated mass change from EQCM (top) and CV traces (bottom) of 0.5 mM solutions of **8b** (left) and **10** (right) in 0.1 M $HClO_4$ at 10 mV s^{-1} at a gold electrode (0.35 cm^2). Black traces indicate the data of the first cycle between 1.2 and 2.0 V vs. RHE, grey lines indicate subsequent 19 cycles.

In a combined CA-EQCM experiment, the deposition of material was measured for continuous electrochemical water oxidation with complexes **8b** and **10** at a fixed potential for 15 minutes (Figure 8). As observed in regular CA measurements in a hanging meniscus configuration (*cf* Figure 6), neither of the two complexes showed any catalytic current when the potential was kept at 1.7 V vs. RHE and also no mass gain was detected. When the potential was raised to 1.8 V vs. RHE, a catalytic cur-

rent was observed for complex **10** which gradually increased over the full duration of the measurement to reach about 0.2 mA after 15 min. The current density is substantially higher for complex **8b** (> 1.0 mA) and was reached already after about 500 s and then plateaued at this level for the remaining 400 s. Associated with the gradually increasing catalytic current of complex **10**, also the oscillation frequency of the EQCM changes and continuously increases, indicating a deposition of approximately 3 μg cm^{-2}. Upon switching off the potential after 900 s, the mass gain reverts largely, suggesting a reversible change of the frequency and hence not a deposition of (typically irreversibly formed) heterogenized iridium oxide catalyst, which has been shown to be irreversibly deposited.[24,75] This effect is even more pronounced for the electrocatalytically much more active complex **8b**. When the potential is kept at 1.8 V vs. RHE, significant amounts of deposition (6.5 μg cm^{-2}) were concluded from the frequency changes, however, this mass gain is almost completely reversed when switching the potential back to 0.7 V vs. RHE (> 75 % desorption). This behavior is not in agreement with decomposition or electrochemical formation of an (inorganic) heterogeneous layer such iridium oxide on the electrode, since electrochemical removal of iridium oxide is very difficult and does not occur at 0.7 V vs. RHE. The increase in weight is therefore attributed to the physisorption of the catalytically active homogeneous species. Such a model also rationalizes the minor differences observed when comparing the experiments carried out in a hanging meniscus configuration vs. a EQCM set-up. It is also interesting to note that the mass changes observed by CA-EQCM for complexes **8b** and **10** differ by a factor 2, while the catalytic current is about 5 times larger for **8b** vs. **10**, which is not compatible with a direct correlation between deposited material and catalytic activity.

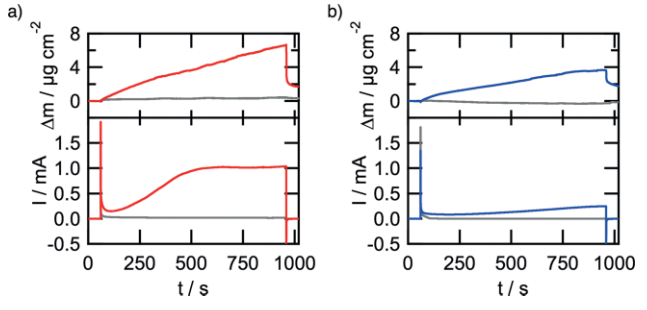

Figure 8. EQCM results from chronoamperometric measurements of complexes **8b** (a) and **10** (b). Potential was held at 0.7 V (0–60 s), 1.7 V (grey, 60–960 s) or 1.8 V (red/blue, 60–960 s) and 0.7 V again (960–1020 s) for 0.5 mM solutions of the corresponding complex **10** in 0.1 M $HClO_4$ electrolyte solution at a gold electrode (0.35 cm^2); all potentials vs. RHE.

Online Electrochemical Mass Spectrometry (OLEMS) Measurements. In addition to EQCM experiments to probe the homogeneous nature of the (modified) complexes, OLEMS[75–77] measurements were performed to provide access to real-time information about the gaseous products that are formed at the electrode surface. Since this technique combines classical electrochemical methods with on-line mass spectrometry, such tandem measurements also shed light on the onset potentials of these reactions and on possible decomposition pathways. Gas product measurement during a CV cycle revealed evolution of oxygen for both complexes **8b** and **10** simultaneous to the increase of catalytic current above 1.8 V vs. RHE (Figure 9). Minute levels of CO_2 were also detected, though the quantities were 2 orders of magnitude lower than oxygen. It is worth noting that CO_2 formation commenced at about 200 mV earlier potential than oxygen evolution. These data are in agreement with (partial) Cp* oxidation as observed in related systems by NMR spectroscopy.[29–33]

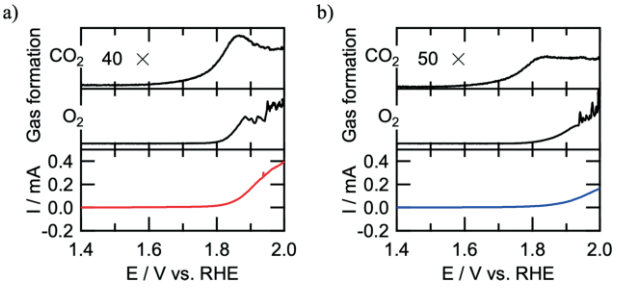

Figure 9. Online spectrometric monitoring of the gas phase of solutions of complexes **8b** (a) and **10** (b) by OLEMS upon electrochemical water oxidation induced by sweeping the potential from 1.4 to 2.0 V vs. RHE (0.1 M $HClO_4$ solution; gold electrode, ν = 1 mV s^{-1}). Top panel: CO_2 evolution; middle panel: O_2 evolution; bottom panel: linear sweep voltammogram.

A combined chronoamperometric/OLEMS experiment of complex **8b** at a fixed potential of 1.8 V vs. RHE shows an immediate evolution of dioxygen and indicates a ca. 300 mV overpotential with respect to the equilibrium potential of water (Figure 10). The dioxygen trace plateaus already after 10 seconds, indicating saturation of the solution around the electrode and the OLEMS inlet (Figure 10c). After saturation the oxygen levels appear to further increase, yet this is most likely due to violent

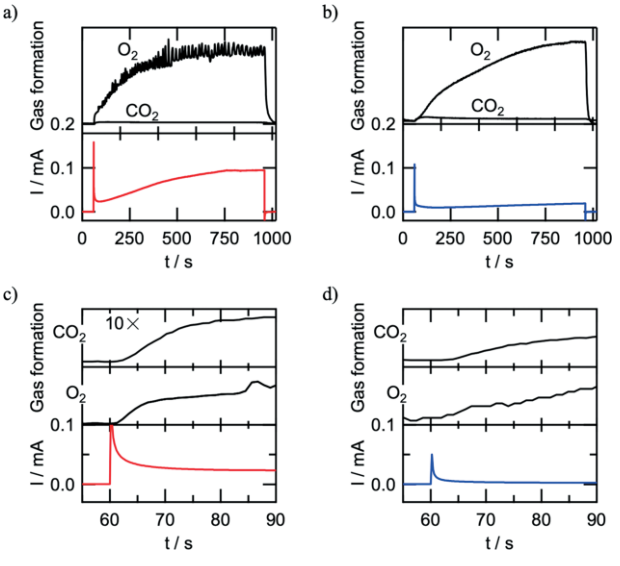

Figure 10. Change of current density and gas evolution upon electrochemical water oxidation with complex **8b** (a) and **10** (b) measured by OLEMS (0.05 cm^2 gold electrode), 0.1 M $HClO_4$ and 0.5 mM solution of iridium complex, potential at 0.7 V (0–60 s), 1.8 V (60–960 s), and 0.7 V (960–1020 s); all potentials vs. RHE. Upper panel: O_2 evolution; middle panel: CO_2 evolution; lower panel: current. Magnifications of the first 60 seconds of reaction for **8b** (c) and **10** (d). $.

bubble formation at the electrode, which gives rise the many spikes on the O_2 trace (Figure 10a). Also, CO_2 is formed immediately albeit at considerably lower levels compare to dioxygen and in contrast to dioxygen, the CO_2 levels decreases over time.

The chronoamperometric/OLEMS trace of complex **10** is remarkably different. The increase of the O_2 levels at the very beginning is very slow and after 120 seconds the dioxygen levels are still increasing, suggesting that activation of the precatalyst to the active species is still taking place (Figure 10b, Figure 10d). In contrast to complex **8b** the observed currents of complex **10** remain roughly a magnitude lower, even after 900 seconds, and formation of oxygen bubbles are never observed, neither in the OLEMS trace nor visibly. This behavior is in full agreement with the data from chronoamperometry, which reveal a 10-fold higher catalytic current of complex **8b** compared to **10** (*cf* Figure 6).[78]

X-ray Photoelectron Spectroscopy. To unambiguously characterize the nature of the "deposite" observed during EQCM measurements, experiments were carried out to investigate the electrode surface when complex **8b** was used for electrochemical water oxidation. The material on the electrode surface after combined CV- and CA-EQCM measurements was investigated *ex situ* by X-ray photoelectron spectroscopy (XPS).

The XPS spectra in the Ir 4f region of the iridium deposits (Figure 11) showed a signal at 62.4 eV which is typical for a molecular iridium(IV) species.[32,79,80] The observed binding energy is considerably lower than IrO_2 systems, which are typically observed above 62.7 eV,[80,81] and higher than the binding energy of Ir_2O_3, which is found below 62.2 eV.[81,82]

In the carbon 1s region, the XPS spectra kept the same signal at 285 eV from the beginning of the experiment and supports

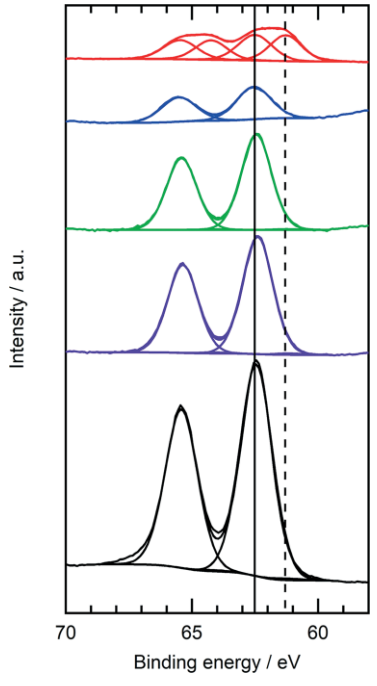

Figure 11. XPS spectrum in the Ir 4f region of the powder complex **8b** (red) and after 1 (blue), 3 (green), 5 (purple) and 10 minutes (black) chronoamperometry of 0.5 mM solutions of **8b** in 0.1 M $HClO_4$ at gold (0.35 cm^2) electrodes.

the integrity of the ligand skeleton (Figure S28). In addition, a new signal at 288 eV appeared after 3 minutes at an energy that may point to a carbonyl group due to C oxidation on the ligand. This observation may be rationalized by a stepwise oxidation of e.g. the Cp* ligand as demonstrated earlier by Macchioni and co-workers.[29,30] Finally, the N 1s region showed that the nitrogen portion of the ligand remained relatively unchanged throughout the experiment, indicating that the deposited material still contains the triazolylidene-pyridyl ligand framework. However, the amount of iridium appears to build up over time, whereas the amounts of carbon and nitrogen increase to a much lesser extent. Apparently, some of the pyridyl-triazolylidene ligand is lost during prolonged amperometry measurements.

Conclusions

We have reported new mesoionic carbene iridium complexes, which are efficient chemical and electrochemical water oxidation catalysts. Here, we show how simple ligand modifications modulate the catalytic activity, which strongly indicates a catalytically active species in which the *C,N*-bidentate coordinating carbene ligand remains coordinated to the iridium center. Most remarkably, the correlation between the catalyst structure and the activation rate of the catalysts differs considerably between chemical oxidation with CAN and upon electrochemical oxidation. While for CAN-driven water oxidation, electron donating groups on both the triazolylidene and pyridyl ligand units enhance catalytic activity, electrochemical catalysis is highest when the triazolylidene is unsubstituted. The relative activity of **10** as the best performing catalyst in CAN-driven processes vs. **8b**, the best electrocatalytic system, reveals a significant divergence with a 2:1 activity ratio in CAN-mediated oxidation compared to a 1:5 ratio in electrochemical water oxidation. While this work provides support for a similar activation of the system via Cp* degradation irrespective of the oxidation method, it is likely that the presence of cerium affects the catalytically active species and hence leads to a different resting state or a different electron transfer mechanism than electrochemical oxidation. Our work indicates that it is very difficult to extrapolate catalytic activity trends gained from experiments using a sacrificial oxidant to water oxidation activity at electrodes. While sacrificial oxidants have often been used for a primary assessment of the quality and efficiency of catalysts, this work here demonstrates that such evaluations need to be interpreted with caution. In particular when considering that ultimately, a device for water splitting will be comprised of a (photovoltaic) electrochemical cell, catalyst evaluation at electrodes will need to be evaluated at early stages to not discard active catalysts such as **8b** that show only mediocre performance in the chemically driven water oxidation but provide excellent electrochemical catalysts.

Experimental Section

General: The metalation reactions were carried out under nitrogen atmosphere using standard Schlenk techniques, and all the reagents and solvents were used as obtained from commercial sources.

The precursor compounds 2-azidopyridine (**1a**),[83] 1-(2-pyridyl)-1,2,3-triazole (**2a**),[84] 5-methoxy-2-(1*H*-1,2,3-triazol-1-yl)-pyridine (**2b**),[84] 4-methoxy-2-(1*H*-1,2,3-triazol-1-yl)-pyridine (**2c**),[84] 4-*N*,*N*-dimethyl-2-(1*H*-1,2,3-triazol-1-yl)pyridinamine (**2e**),[84] ethyl 1-(2-pyridyl)-1*H*-1,2,3-triazole-4-carboxylate (**3a**),[85] triazolium salts **5a**,[69] and **6a**,[86] as well as iridium complex **8a**,[69] and [IrCp*Cl2]2[87] were prepared according to literature procedures. All other ligand precursors are described in the supporting information. Unless specified otherwise, NMR spectra were recorded at 25 °C on Varian spectrometers operating at 300, 400 or 500 MHz (^{1}H NMR), and 100 MHz (^{13}C{^{1}H} NMR) respectively or on Bruker spectrometers operating at 300 or 400 MHz (^{1}H NMR) and 75 or 100 MHz (^{13}C{^{1}H} NMR) respectively. Chemical shifts (δ in ppm, coupling constants *J* in Hz) were referenced to residual solvent signals (^{1}H, ^{13}C). Assignments are based on homo- and heteronuclear shift correlation spectroscopy. All complexes show a quartet around 120 ppm in the ^{13}C NMR spectrum due to the OTf counterion. Elemental analyses were performed by the microanalytical laboratories of University College Dublin and the University of Bern.

General Procedure for the Synthesis of the Complexes 8b, 9a–c, 10 and 11: Compound **5b**, **6a**–**c**, and **7** (1 equiv.) and $[IrCp^*Cl_2]_2$ (0.5 equiv.) were suspended in degassed toluene (15 mL) and stirred at 120 °C for the indicated time. The solvent was removed and the residue was dissolved in CH_3CN and layered with Et_2O to precipitate a yellow solid, which was dried under reduced pressure affording the complex (**8b**, **9a**–**c**, **10** and **11**). The residue was purified via column chromatography (SiO_2; CH_2Cl_2/acetone).

General Procedure for the Synthesis of the Complexes 8c–e: Compound **5c**–**e**, (1 equiv.) and $[IrCp^*Cl_2]_2$ (0.5 equiv.) were solved in degassed toluene (5 mL) and heated in a closed vial at 140 °C for 4 h. After cooling to ambient temperature, the suspension was filtered through Celite and the insoluble parts were solved in CH_3CN (5 mL). The complex was precipitated from the solution by addition of Et_2O (100 mL), collected by decantation and dried under reduced pressure to yield the complex (**8c–e**).

Complex 8b: Reaction of **5b** (145 mg, 0.43 mmol) and $[IrCp^*Cl_2]_2$ (170 mg, 0.21 mmol) was stirred for 48 h, according to the general procedure gave **8b** as a yellow solid (250 mg, 84 %). ^{1}H NMR (400 MHz, $CDCl_3$): δ = 8.37 (s, 1H, $C_{trz}H$), 8.25 (d, $^4J_{HH}$ = 2.7 Hz, 1H, $C_{py}H$), 8.13 (d, $^3J_{HH}$ = 9.1 Hz, 1H, $C_{py}H$), 7.71 (dd, $^3J_{HH}$ = 9.1 Hz, $^4J_{HH}$ = 2.7 Hz, 1H, $C_{py}H$), 4.45 (s, 3H, NCH_3), 4.03 (s, 3H, OCH_3), 1.84 (s, 15H, $C_{Cp^*}H_3$). ^{13}C{^{1}H} NMR (100 MHz, $CDCl_3$): δ = 157.8 (C_{py}-OMe), 153.6 (C_{trz}-Ir), 143.9 (C_{py}-N_{trz}), 139.2 ($C_{py}H$), 133.4 ($C_{trz}H$), 125.3 ($C_{py}H$), 115.1 ($C_{py}H$), 91.7 (C_{Cp^*}), 57.0 (OCH_3), 40.2 (NCH_3), 9.4 ($C_{Cp^*}H_3$). Anal. Calcd for $C_{20}H_{25}ClF_3IrN_4O_4S$ (702.17): C, 34.21; H, 3.59; N, 7.98; found C, 34.13; H, 3.60; N, 8.05. HR-MS (CH_3CN): *m/z* calculated for $C_{19}H_{25}ON_4ClIr$ [M – OTf]$^+$ = 553.1341; found 553.1333.

Complex 8c: Reaction of **5c** (50 mg, 0.147 mmol) and $[IrCp^*Cl_2]_2$ (60 mg, 0.074 mmol) was stirred for 4 h at 140 °C according to the general procedure yielding **8c** as a yellow solid (45 mg, 86 %). ^{1}H NMR (600 MHz, CD_3CN): δ = 8.48 (d, $^3J_{HH}$ = 6.6 Hz, 1H, $C_{py}H$), 8.15 (s, 1H, $C_{trz}H$), 7.67 (d, $^4J_{HH}$ = 2.7 Hz, 1H, $C_{py}H$), 7.22 (dd, $^3J_{HH}$ = 6.6 Hz, $^4J_{HH}$ = 2.7 Hz, 1H, $C_{py}H$), 4.33 (s, 3H, NCH_3), 4.07 (s, 3H, OCH_3), 1.77 (s, 15H, $C_{Cp^*}H_3$). ^{13}C{^{1}H} NMR (125 MHz, CD_3CN): δ = 170.8 (C_{py}-OMe), 156.7 (C_{trz}-Ir), 153.2 ($C_{py}H$), 152.4 (C_{py}-N_{trz}), 133.7 ($C_{trz}H$), 114.9 ($C_{py}H$), 100.8 ($C_{py}H$), 92.0 (C_{Cp^*}), 58.3 (OCH_3), 40.7 (NCH_3), 9.4 ($C_{Cp^*}H_3$). Anal. Calcd for $C_{20}H_{25}ClF_3IrN_4O_4S$ (702.17): C, 34.21; H, 3.59; N, 7.98; found C, 34.01; H, 3.34; N, 7.90. HR-MS (CH_3CN): *m/z* calculated for $C_{19}H_{25}ON_4ClIr$ [M – OTf]$^+$ = 553.1341; found 553.1348.

Complex 8d: Reaction of **5d** (20 mg, 0.055 mmol) and $[IrCp^*Cl_2]_2$ (22 mg, 0.028 mmol) was stirred for 4 h at 140 °C according to the general procedure yielding **8d** as a yellow solid (35 mg, 87 %). ^{1}H NMR (400 MHz, CD_3CN): δ = 8.61 (dd, $^3J_{HH}$ = 6.1 Hz, $^5J_{HH}$ = 0.5 Hz, 1H, $C_{py}H$), 8.17 (s, 1H, $C_{trz}H$), 8.15 (dd, $^4J_{HH}$ = 2.0 Hz, $^5J_{HH}$ = 0.5 Hz, 1H, $C_{py}H$), 7.71 (dd, $^3J_{HH}$ = 6.1 Hz, $^4J_{HH}$ = 2.0 Hz, 1H, $C_{py}H$), 4.35 (s, 3H, NCH_3), 1.78 (s, 15H, $C_{Cp^*}H_3$), 1.42 (s, 9H, CH_3). ^{13}C{^{1}H} NMR (100 MHz, CD_3CN): δ = 168.7 (C_{tBu}-CH_3), 156.3 (C_{trz}-Ir), 152.3 ($C_{py}H$), 151.0 (C_{py}-N_{trz}), 133.6 ($C_{trz}H$), 125.7 ($C_{py}H$), 112.0 ($C_{py}H$), 92.3 (C_{Cp^*}), 40.7 (NCH_3), 36.8 (C_{py}-*t*Bu), 30.3 (CH_3), 9.4 ($C_{Cp^*}H_3$). Anal. Calcd for $C_{23}H_{31}ClF_3IrN_4O_3S$ (728.25): C, 37.93; H, 4.29; N, 7.69; found C, 38.06; H, 4.11; N, 7.97. HR-MS (CH_3CN): *m/z* calculated for $C_{22}H_{31}N_4ClIr$ [M – OTf]$^+$ = 579.1867; found 579.1854.

Complex 8e: Reaction of **5e** (50 mg, 0.142 mmol) and $[IrCp^*Cl_2]_2$ (56 mg, 0.070 mmol) was stirred for 4 h at 140 °C according to the general procedure yielding **8e** as a yellow solid (70 mg, 70 %). ^{1}H NMR (400 MHz, CD_3CN): δ = 8.10 (d, $^3J_{HH}$ = 7.0 Hz, 1H, $C_{py}H$), 8.07 (s, 1H, $C_{trz}H$), 7.19 (d, $^4J_{HH}$ = 2.9 Hz, 1H, $C_{py}H$), 6.78 (dd, $^3J_{HH}$ = 7.0 Hz, $^4J_{HH}$ = 2.9 Hz, 1H, $C_{py}H$), 4.30 (s, 3H, NCH_3), 3.19 (s, 6H, $N(CH_3)_2$), 1.76 (s, 15H, $C_{Cp^*}H_3$). ^{13}C{^{1}H} NMR (100 MHz, CD_3CN): δ = 157.4 (C_{py}-NMe_2), 155.8 (C_{trz}-Ir), 151.0 (C_{py}-N_{trz}), 150.4 ($C_{py}H$), 133.3 ($C_{trz}H$), 110.2 ($C_{py}H$), 95.6 ($C_{py}H$), 91.4 (C_{Cp^*}), 40.5 (NCH_3), 40.3 ($N(CH_3)_2$), 9.4 ($C_{Cp^*}H_3$). Anal. Calcd for $C_{21}H_{28}ClF_3IrN_5O_3S$ (715.21): C, 35.27; H, 3.95; N, 9.79; found C, 35.61; H, 3.65; N, 9.79. HR-MS (CH_3CN): *m/z* calculated for $C_{20}H_{28}N_5ClIr$ [M – OTf]$^+$ = 566.1663; found 566.1635.

Complex 9a: Reaction of **6a** (200 mg, 0.52 mmol) and $[IrCp^*Cl_2]_2$ (210 mg, 0.26 mmol) was stirred for 24 h, according to the general procedure gave **9a** as a yellow solid (268 mg, 70 %). ^{1}H NMR (400 MHz, $CDCl_3$): δ = 8.65 (d, $^3J_{HH}$ = 5.5 Hz, 1H, $C_{py}H$), 8.32 (d, $^3J_{HH}$ = 8.0 Hz, 1H, $C_{py}H$), 8.17 (td, $^3J_{HH}$ = 8.0 Hz, $^4J_{HH}$ = 1.4 Hz, 1H, $C_{py}H$), 7.63 (ddd, $^3J_{HH}$ = 8.0 Hz, $^3J_{HH}$ = 5.5 Hz, $^4J_{HH}$ = 1.4 Hz, 1H, $C_{py}H$), 4.59 (s, 3H, NCH_3), 4.53 (m, 2H, OCH_2Me), 1.74 (s, 15H, $C_{Cp^*}H_3$), 1.48 (t, $^3J_{HH}$ = 7.1 Hz, 3H, OCH_2CH_3). ^{13}C{^{1}H} NMR (100 MHz, $CDCl_3$): δ = 160.3 (C_{trz}-Ir), 157.2 (C=O), 150.5 ($C_{py}H$), 150.4 (C_{py}-N_{trz}), 142.0 ($C_{py}H$), 136.7 (C_{trz}-COOEt), 127.0 ($C_{py}H$), 115.3 ($C_{py}H$), 92.8 (C_{Cp^*}), 63.2 (OCH_2Me), 43.0 (NCH_3), 14.4 (OCH_2CH_3), 9.3 ($C_{Cp^*}H_3$). Anal. Calcd for $C_{22}H_{27}ClF_3IrN_4O_5S$ (744.20): C, 35.51; H, 3.66; N, 7.53; found C, 35.33; H, 3.81; N, 7.56. HR-MS (CH_3CN): *m/z* calculated for $C_{21}H_{27}O_2N_4ClIr$ [M – OTf]$^+$ = 595.1446; found 595.1460.

Complex 9b: Reaction of **6b** (235 mg, 0.57 mmol) and $[IrCp^*Cl_2]_2$ (226 mg, 0.28 mmol) was stirred for 6 days, according to the general procedure gave **9b** as a yellow solid (341 mg, 78 %). ^{1}H NMR (400 MHz, $CDCl_3$): δ = 8.26 (dd, $^3J_{HH}$ = 8.9 Hz, 1H, $C_{py}H$), 8.26 (dd, $^4J_{HH}$ = 2.7 Hz, 1H, $C_{py}H$), 7.70 (dd, $^3J_{HH}$ = 8.9 Hz, $^4J_{HH}$ = 2.7 Hz, 1H, $C_{py}H$), 4.57 (s, 3H, NCH_3), 4.52 (m, 2H, OCH_2Me), 4.02 (s, 3H, OCH_3), 1.78 (s, 15H, $C_{Cp^*}H_3$), 1.48 (t, $^3J_{HH}$ = 7.1 Hz, 3H, OCH_2CH_3). ^{13}C{^{1}H} NMR (100 MHz, $CDCl_3$): δ = 158.4 (C_{trz}-Ir), 158.0 (C_{py}-OMe), 157.2 (C=O), 143.5 (C_{py}-N_{trz}), 138.6 ($C_{py}H$), 136.5 (C_{trz}-COOEt), 125.6 ($C_{py}H$), 115.7 ($C_{py}H$), 92.6 (C_{Cp^*}), 63.1 (OCH_2Me), 57.0 (OCH_3), 42.7 (NCH_3), 14.4 (OCH_2CH_3), 9.2 ($C_{Cp^*}H_3$). Anal. Calcd for $C_{23}H_{29}ClF_3IrN_4O_6S$ (774.23): C, 35.68; H, 3.78; N, 7.24; found C, 35.50; H, 4.02; N, 6.91. HR-MS (CH_3CN): *m/z* calculated for $C_{22}H_{29}O_3N_4ClIr$ [M – OTf]$^+$ = 625.1552; found 625.1563.

Complex 9c: Reaction of **6c** (235 mg, 0.57 mmol) and $[IrCp^*Cl_2]_2$ (226 mg, 0.28 mmol) was stirred for 48 h according to the general procedure gave **9c** as a yellow solid (278 mg, 63 %). ^{1}H NMR (300 MHz, $CDCl_3$): δ = 8.36 (d, $^3J_{HH}$ = 6.6 Hz, 1H, $C_{py}H$), 7.80 (d, $^4J_{HH}$ = 2.6 Hz, 1H, $C_{py}H$), 7.13 (dd, $^3J_{HH}$ = 6.6 Hz, $^4J_{HH}$ = 2.6 Hz, 1H, $C_{py}H$), 4.61 (s, 3H, NCH_3), 4.55 (m, 2H, OCH_2Me), 4.10 (s, 3H, OCH_3), 1.77 (s, 15H, $C_{Cp^*}H_3$), 1.48 (t, $^3J_{HH}$ = 7.1 Hz, 3H, OCH_2CH_3). ^{13}C{^{1}H} NMR (75 MHz, $CDCl_3$): δ = 169.9 (C_{py}-OMe), 160.5 (C_{trz}-Ir), 157.2 (C=O), 151.6 (C_{py}-N_{trz}), 150.4 ($C_{py}H$), 136.7 (C_{trz}-COOEt), 115.0 ($C_{py}H$), 100.3 ($C_{py}H$), 92.3 (C_{Cp^*}), 63.2 (OCH_2Me), 57.5 (OCH_3), 42.9 (NCH_3), 14.4 (OCH_2CH_3), 9.3 ($C_{Cp^*}H_3$). Anal. Calcd for $C_{23}H_{29}ClF_3IrN_4O_6S$

(774.23): C, 35.68; H, 3.78; N, 7.24; found C, 35.62; H, 3.47; N, 7.26. HR-MS (CH_3CN): *m/z* calculated for $C_{22}H_{29}O_3N_4ClIr$ $[M - OTf]^+$ = 625.1552; found 625.1582.

Complex 10: Reaction of **7** (175 mg, 0.45 mmol) and $[IrCp^*Cl_2]_2$ (180 mg, 0.23 mmol) was stirred for 24 h according to the general procedure gave **10** as a yellow solid (240 mg, 70 %). ^1H NMR (400 MHz, $CDCl_3$): δ = 8.23 (d, $^4J_{HH}$ = 2.7 Hz, 1H, $C_{py}H$), 8.22 (d, $^3J_{HH}$ = 9.1 Hz, 1H, $C_{py}H$), 7.77 (dd, $^3J_{HH}$ = 9.1 Hz, $^4J_{HH}$ = 2.7 Hz, 1H, $C_{py}H$), 4.47 (m, 1H, OCH_2Me), 4.28 (m, 1H, OCH_2Me), 4.19 (s, 3H, NCH_3), 4.02 (s, 3H, OCH_3), 1.82 (s, 15H, $C_{Cp^*}H_3$), 1.46 (t, $^3J_{HH}$ = 7.1 Hz, 3H, OCH_2CH_3). $^{13}C\{^1H\}$ NMR (100 MHz, $CDCl_3$): δ = 158.0 (C_{py}-OMe), 156.4 (C_{trz}-OEt), 144.2 (C_{py}-N_{trz}), 139.0 ($C_{py}H$), 138.0 (C_{trz}-Ir), 125.6 ($C_{py}H$), 115.3 ($C_{py}H$), 91.5 (C_{Cp^*}), 74.8 (OCH_2Me), 57.0 (OCH_3), 35.5 (NCH_3), 15.3 (OCH_2CH_3), 9.4 ($C_{Cp^*}H_3$). Anal. Calcd for $C_{22}H_{29}ClF_3IrN_4O_5S$ (746.22): C, 35.41; H, 3.92; N, 7.51; found C, 35.24; H, 3.96; N, 7.49. HR-MS (CH_3CN): *m/z* calculated for $C_{21}H_{29}O_2N_4ClIr$ $[M - OTf]^+$ = 597.1603; found 597.1616.

Complex 11: A yellow solid precipitated in the solvent portion removed from the reaction of complex **10**. This solid was complex **11** which contains a –OH group on the triazole (26 mg, 8 %). ^1H NMR (400 MHz, $CDCl_3$): δ = 8.26 (d, $^4J_{HH}$ = 2.6 Hz, 1H, $C_{py}H$), 8.04 (d, $^3J_{HH}$ = 8.9 Hz, 1H, $C_{py}H$), 7.65 (dd, $^3J_{HH}$ = 8.9 Hz, $^4J_{HH}$ = 2.6 Hz, 1H, $C_{py}H$), 4.21 (s, 3H, NCH_3), 4.02 (s, 3H, OCH_3), 1.87 (s, 15H, $C_{Cp^*}H_3$). $^{13}C\{^1H\}$ NMR (100 MHz, $CDCl_3$): δ = 157.6 (C_{py}-OMe), 155.0 (C_{trz}-OH), 144.8 (C_{py}-N_{trz}), 138.6 ($C_{py}H$), 137.1 (C_{trz}-Ir), 125.0 ($C_{py}H$), 114.4 ($C_{py}H$), 91.5 (C_{Cp^*}), 56.9 (OCH_3), 35.6 (NCH_3), 9.6 ($C_{Cp^*}H_3$). Anal. Calcd for $C_{20}H_{25}ClF_3IrN_4O_5S$ (718.16): C, 33.45; H, 3.51; N, 7.80; found C, 33.40; H, 3.93; N, 7.73. HR-MS (CH_3CN): *m/z* calculated for $C_{19}H_{25}O_2N_4ClIr$ $[M - OTf]^+$ = 569.1290; found 569.1298.

General Procedure for the Synthesis of the Complexes 12a–c: 9a–c: (1 equiv.) and lithium hydroxide monohydrate (2 equiv.), were dissolved in a mixture of MeOH and water (6 mL and 3 mL). The reaction was stirred at room temperature for 3 h. 1 M HCl aqueous solution was added dropwise until pH = 3–5 was reached. The reaction was extracted with brine (2x 10 mL) and CH_2Cl_2 (5x 15 mL). The organic layer was dried with $MgSO_4$ and the solvent was removed under reduced pressure. Residue was dissolved in CH_2Cl_2 and layered with Et_2O to precipitate a yellow solid, which was dried under reduced pressure affording the complex (**12a**–**c**).

Complex 12a: Reaction of **9a** (130 mg, 0.17 mmol) and lithium hydroxide monohydrate (15 mg, 0.35 mmol) according to the general procedure gave **12a** as a yellow solid (95 mg, 78 %). ^1H NMR (400 MHz, $CDCl_3$): δ = 8.71 (d, $^3J_{HH}$ = 5.5 Hz, 1H, $C_{py}H$), 8.27 (m, 2H, $C_{py}H$), 7.75 (m, 1H, $C_{py}H$), 4.59 (s, 3H, NCH_3), 1.82 (s, 15H, $C_{Cp^*}H_3$). $^{13}C\{^1H\}$ NMR (100 MHz, $CDCl_3$): δ = 160.0 (C=O), 155.3 (C_{trz}-Ir), 151.0 ($C_{py}H$), 150.2 (C_{py}-N_{trz}), 142.3 ($C_{py}H$), 142.0 (C_{trz}-COOH), 127.5 ($C_{py}H$), 114.6 ($C_{py}H$), 92.5 (C_{Cp^*}), 41.3 (NCH_3), 9.5 ($C_{Cp^*}H_3$). Anal. Calcd for a mixture 1:1 complex with and without counterion $C_{39}H_{45}Cl_2F_3Ir_2N_8O_7S$ (1282.23): C, 36.53; H, 3.54; N, 8.74; found C, 36.39; H, 3.84; N, 8.29. HR-MS (CH_3CN): *m/z* calculated for $C_{19}H_{23}O_2N_4ClIr$ $[M - OTf]^+$ = 567.1133; found 567.1126.

Complex 12b: Reaction of **9b** (130 mg, 0.17 mmol) and lithium hydroxide monohydrate (15 mg, 0.35 mmol) according to the general procedure gave **12b** as a yellow solid (90 mg, 72 %). ^1H NMR (400 MHz, $CDCl_3$): δ = 8.28 (d, $^4J_{HH}$ = 2.6 Hz, 1H, $C_{py}H$), 8.06 (d, $^3J_{HH}$ = 9.1 Hz, 1H, $C_{py}H$), 7.70 (dd, $^3J_{HH}$ = 9.1 Hz, $^4J_{HH}$ = 2.6 Hz, 1H, $C_{py}H$), 4.50 (s, 3H, NCH_3), 4.01 (s, 3H, OCH_3), 1.83 (s, 15H, $C_{Cp^*}H_3$). $^{13}C\{^1H\}$ NMR (100 MHz, $CDCl_3$): δ = 160.0 (C=O), 157.5 (C_{py}-OMe), 150.2 (C_{trz}-Ir), 146.1 (C_{trz}-COOH), 144.2 (C_{py}-N_{trz}), 138.3 ($C_{py}H$), 125.4 ($C_{py}H$), 114.6 ($C_{py}H$), 91.9 (C_{Cp^*}), 57.0 (OCH_3), 39.9 (NCH_3), 9.4 ($C_{Cp^*}H_3$). Anal. Calcd for a mixture 1:1 complex with and without counterion $C_{41}H_{49}Cl_2F_3Ir_2N_8O_9S$ (1342.28): C, 36.69; H, 3.68; N, 8.35; found C, 36.86; H, 3.85; N, 8.31. HR-MS (CH_3CN): *m/z* calculated for $C_{20}H_{25}O_3N_4ClIr$ $[M - OTf]^+$ = 597.1239; found 597.1227.

Complex 12c: Reaction of **9c** (80 mg, 0.10 mmol) and lithium hydroxide monohydrate (10 mg, 0.20 mmol) according to the general procedure gave **12c** as a yellow solid (50 mg, 67 %). ^1H NMR (400 MHz, $CDCl_3$): δ = 8.47 (d, $^3J_{HH}$ = 5.7 Hz, 1H, $C_{py}H$), 7.67 (s, 1H, $C_{py}H$), 7.29 (d, $^3J_{HH}$ = 5.7 Hz, 1H, $C_{py}H$), 4.58 (s, 3H, NCH_3), 4.12 (s, 3H, OCH_3), 1.80 (s, 15H, $C_{Cp^*}H_3$). $^{13}C\{^1H\}$ NMR (100 MHz, $CDCl_3$): δ = 169.7 (C_{py}-OMe), 160.0 (C=O), 156.0 (C_{trz}-Ir), 151.4 (C_{py}-N_{trz}), 151.3 ($C_{py}H$), 141.4 (C_{trz}-COOH), 114.5 ($C_{py}H$), 100.3 ($C_{py}H$), 92.0 (C_{Cp^*}), 57.7 (OCH_3), 41.4 (NCH_3), 9.5 ($C_{Cp^*}H_3$). Anal. Calcd for $C_{21}H_{25}ClF_3IrN_4O_6S$ (746.17): C, 33.80; H, 3.38; N, 7.51; found C, 34.13; H, 3.52; N, 7.54. HR-MS (CH_3CN): *m/z* calculated for $C_{20}H_{25}O_3N_4ClIr$ $[M - OTf]^+$ = 597.1239; found 597.1247.

Catalytic Water Oxidation Using CAN: An aqueous solution of the iridium complex was injected into a 20 mL EPA vial sealed with a customized cap containing 10 mL of 0.37 M CAN solution buffered in 1 M HNO_3. O_2 evolution was monitored with pressure transducers and the end point oxygen content in the headspace of the reaction was verified by GC analysis.

Electrochemical Methods: All electrochemical and EQCM experiments were performed on an Autolab PGSTAT 128N. All electrochemical experiments were performed in one-compartment 25 mL glass cells in a three-electrode setup, using an ITO working electrode (0.35 cm^2 geometric surface area) or a gold working electrode (0.05 cm^2 geometric surface area, WE). A gold wire was used as a counter electrode and all experiments were measured against the reversible hydrogen electrode (RHE). The electrochemical cell was boiled twice in Millipore MilliQ water (> 18.2 MΩ cm resistivity) prior to the experiment. The ITO working electrode was cleaned by sonicating twice in 2-propanol (Honeywell, reagent grade) for 20 min, followed by sonication in MilliQ water (> 18.2 MΩ cm resistivity). The electrode (50 × 7 mm) was lowered 5 mm into the electrolyte solution, resulting in an active electrode surface of 5 × 7 mm. The Au WE consisted of a disc and was used in a hanging meniscus configuration. The WE was cleaned by applying 10 V between the WE and a graphite counter electrode for 30 s in a 10 % H_2SO_4 solution. This was followed by dipping the WE in a 6 M HCl solution for 20 s. The electrode was flame annealed, followed by electrochemical polishing in 0.1 M $HClO_4$, while scanning between 0 and 1.75 V vs. RHE for 200 cycles at 1 V s^{-1}. The electrolyte solutions were prepared from MilliQ water (> 18.2 MΩ cm resistivity) and $HClO_4$ (Merck, Suprapur). The catalysts (0.5 mM) were dissolved in 0.1 M $HClO_4$ electrolyte solutions.

The electrochemical quartz crystal microbalance (EQCM) experiments were performed in a 3 mL Teflon cell purchased from Autolab. As a working electrode, an Autolab EQCM electrode was used, wherein a 200 nm gold layer (0.35 cm^2 geometric surface area) was deposited on a quartz crystal. A custom-made RHE was used that allowed for a stable EQCM signal. Calibration details of the EQCM can be found elsewhere.[88]

During the online electrochemical mass spectrometry (OLEMS) measurements the gaseous products formed at the working electrode were collected via a hydrophobic tip (KEL-F with a porous Teflon plug) in close proximity to the surface of the working electrode and analyzed in a Pfeiffer QMS 200 mass spectrometer. An Ivium A06075 potentiostat was used in combination with the OLEMS experiments. A detailed description of the OLEMS setup is available elsewhere.[76]

X-ray Photoelectron Spectroscopy: XPS measurements were carried out with a Thermo Scientific K-Alpha, equipped with a mono-

chromatic small-spot X-ray source and a 180° double focusing hemispherical analyzer with a 128-channel detector. Spectra were obtained using an aluminium anode (Al-K_α = 1486.6 eV) operating at 72 W and a spot size of 400 µm. Survey scans were measured at a constant pass energy of 200 eV and region scans at 50 eV. The background pressure was 2×10^{-8} mbar and during measurement 4×10^{-7} mbar Argon because of charge compensation.

Samples for XPS were prepared by chrono amperometry at gold working electrodes with 0.5 mM of **8b** in 0.1 M $HClO_4$ electrolyte solutions at 1.8 V vs. RHE. Samples were prepared by applying oxidative potentials for 1, 3, 5 or 10 minutes.

Crystal Structure Determinations: Crystal data for **8b**, **8d**, **8e**, **9a**, **9b**, **9c**, **10**, **11**, **12a**, and **12b** were collected using a Rigaku (former Agilent Technologies) Oxford Diffraction SuperNova A diffractometer fitted with an Atlas detector.[89] **8e** and **9b** were measured with Cu-K_α radiation (1.54184 Å). All other complexes were measured with Mo-K_α radiation (0.71073 Å). For **8b**, **10**, and **11** the radiation was Al filtered.[90] A complete dataset was collected, assuming that the Friedel pairs are not equivalent. Data reduction was performed using the CrysAlisPro program. The intensities were corrected for Lorentz and polarization effects, and numerical absorption correction based on gaussian integration over a multifaceted crystal model was applied. The structures were solved by direct methods using SHELXS,[91] which revealed the positions of all not disordered non-hydrogen atoms. The non-hydrogen atoms were refined anisotropically. All H-atoms were placed in geometrically calculated positions and refined using a riding model where each H-atom was assigned a fixed isotropic displacement parameter with a value equal to 1.2Ueq of its parent atom (1.5Ueq for the methyl groups and water). Refinement of the structure was carried out on F^2 using full-matrix least-squares procedures, which minimized the function $\Sigma w(F_o^2 - F_c^2)^2$. The weighting scheme was based on counting statistics and included a factor to downweight the intense reflections. All calculations were performed using the SHELXL-2014/7 (**8b**, **10**, **11**) or SHELXL97–2 (all others) program.[92] Further crystallographic details are compiled in Tables S1–10.

CCDC 1909354 (for **8b**), 1909357 (for **8d**), 1909356 (for **8e**), 1909363 (for **9a**), 109361 (for **9b**), 1909359 (for **9c**), 1909360 (for **10**), 1909355 (for **11**), 1909358 (for **12a**), and 1909362 (for **12b**) contain the supplementary crystallographic data for this paper. These data can be obtained free of charge from The Cambridge Crystallographic Data Centre.

Supporting Information (see footnote on the first page of this article): Synthesis of new ligand precursors; NMR spectra of all new compounds; crystallographic details; oxygen evolution traces of all compounds; X-ray photoelectron spectra; electrochemical measurements.

Acknowledgments

This work has been financially supported by the European Research Council (CoG 615653 to M. A.), the Swiss National Science Foundation (200020_182663), the US NSF (CHE-1764353 to S. B.) and by Carnegie Mellon's Manufacturing Futures Initiative that is funded by the Richard King Mellon Foundation.

Keywords: Iridium · Water oxidation · Chemical oxidant · Electrocatalysis · Structure activity relationship

[1] N. S. Lewis, D. G. Nocera, *Proc. Natl. Acad. Sci. USA* **2006**, *103*, 15729–15735.
[2] J. J. Concepcion, R. L. House, J. M. Papanikolas, T. J. Meyer, *Proc. Natl. Acad. Sci. USA* **2012**, *109*, 15560–15564.
[3] D. Gust, T. A. Moore, A. L. Moore, *Acc. Chem. Res.* **2009**, *42*, 1890–1898.
[4] S. Berardi, S. Drouet, L. Francàs, C. Gimbert-Suriñach, M. Guttentag, C. Richmond, T. Stoll, A. Llobet, *Chem. Soc. Rev.* **2014**, *43*, 7501–7519.
[5] Z. Han, W. R. McNamara, M. S. Eum, P. L. Holland, R. Eisenberg, *Angew. Chem. Int. Ed.* **2012**, *51*, 1667–1670; *Angew. Chem.* **2012**, *124*, 1699.
[6] W. R. McNamara, Z. Han, P. J. Alperin, W. W. Brennessel, P. L. Holland, R. Eisenberg, *J. Am. Chem. Soc.* **2011**, *133*, 15368–15371.
[7] Z. Han, F. Qiu, R. Eisenberg, P. L. Holland, T. D. Krauss, *Science* **2012**, *338*, 1321–1324.
[8] C. G. Morales-Guio, L. A. Stern, X. Hu, *Chem. Soc. Rev.* **2014**, *43*, 6555–6569.
[9] N. D. McDaniel, S. Bernhard, *Dalton Trans.* **2010**, *39*, 10021–10030.
[10] M. D. Kärkäs, O. Verho, E. V. Johnston, B. Åkermark, *Chem. Rev.* **2014**, *114*, 11863–12001.
[11] J. D. Blakemore, R. H. Crabtree, G. W. Brudvig, *Chem. Rev.* **2015**, *115*, 12974–13005.
[12] S. W. Gersten, G. J. Samuels, T. J. Meyer, *J. Am. Chem. Soc.* **1982**, *104*, 4029–4030.
[13] C. Sens, I. Romero, M. Rodríguez, A. Llobet, T. Parella, J. Benet-Buchholz, *J. Am. Chem. Soc.* **2004**, *126*, 7798–7799.
[14] N. D. McDaniel, F. J. Coughlin, L. L. Tinker, S. Bernhard, *J. Am. Chem. Soc.* **2008**, *130*, 210–217.
[15] J. F. Hull, D. Balcells, J. D. Blakemore, C. D. Incarvito, O. Eisenstein, G. W. Brudvig, R. H. Crabtree, *J. Am. Chem. Soc.* **2009**, *131*, 8730–8731.
[16] J. L. Fillol, Z. Codolà, I. Garcia-Bosch, L. Gómez, J. J. Pla, M. Costas, *Nat. Chem.* **2011**, *3*, 807–13.
[17] J. B. Gerken, J. G. McAlpin, J. Y. C. Chen, M. L. Rigsby, W. H. Casey, R. D. Britt, S. S. Stahl, *J. Am. Chem. Soc.* **2011**, *133*, 14431–14442.
[18] F. Evangelisti, R. Moré, F. Hodel, S. Luber, G. R. Patzke, *J. Am. Chem. Soc.* **2015**, *137*, 11076–11084.
[19] H. Lv, J. Song, Y. V. Geletii, J. W. Vickers, J. M. Sumliner, D. G. Musaev, P. Kögerler, P. F. Zhuk, J. Bacsa, G. Zhu, C. L. Hill, *J. Am. Chem. Soc.* **2014**, *136*, 9268–9271.
[20] W. C. Ellis, N. D. McDaniel, S. Bernhard, T. J. Collins, *J. Am. Chem. Soc.* **2010**, *132*, 10990–10991.
[21] M. Wiechen, H. M. Berends, P. Kurz, *Dalton Trans.* **2012**, *41*, 21–31.
[22] L. Duan, F. Bozoglian, S. Mandal, B. Stewart, T. Privalov, A. Llobet, L. Sun, *Nat. Chem.* **2012**, *4*, 418–423.
[23] Z. Codola, J. M. S. Cardoso, B. Royo, M. Costas, J. Lloret-Fillol, *Chem. Eur. J.* **2013**, *19*, 7203–7213.
[24] N. D. Schley, J. D. Blakemore, N. K. Subbaiyan, C. D. Incarvito, F. Dsouza, R. H. Crabtree, G. W. Brudvig, *J. Am. Chem. Soc.* **2011**, *133*, 10473–10481.
[25] A. Macchioni, *Eur. J. Inorg. Chem.* **2019**, 7–17.
[26] J. A. Woods, R. Lalrempuia, A. Petronilho, N. D. McDaniel, H. Müller-Bunz, M. Albrecht, S. Bernhard, *Energy Environ. Sci.* **2014**, *7*, 2316–2328.
[27] A. Petronilho, J. A. Woods, S. Bernhard, M. Albrecht, *Eur. J. Inorg. Chem.* **2014**, 708–714.
[28] D. B. Grotjahn, D. B. Brown, J. K. Martin, D. C. Marelius, M. C. Abadjian, H. N. Tran, G. Kalyuzhny, K. S. Vecchio, Z. G. Specht, S. A. Cortes-Llamas, V. Miranda-Soto, C. van Niekerk, C. E. Moore, A. L. Rheingold, *J. Am. Chem. Soc.* **2011**, *133*, 19024–19027.
[29] C. Zuccaccia, G. Bellachioma, O. Bortolini, A. Bucci, A. Savini, A. Macchioni, *Chem. Eur. J.* **2014**, *20*, 3446–3456.
[30] A. Savini, P. Belanzoni, G. Bellachioma, C. Zuccaccia, D. Zuccaccia, A. Macchioni, *Green Chem.* **2011**, *13*, 3360–3374.
[31] A. J. Ingram, A. B. Wolk, C. Flender, J. Zhang, C. J. Johnson, U. Hintermair, R. H. Crabtree, M. A. Johnson, R. N. Zare, *Inorg. Chem.* **2014**, *53*, 423–433.
[32] U. Hintermair, S. W. Sheehan, A. R. Parent, D. H. Ess, D. T. Richens, P. H. Vaccaro, G. W. Brudvig, R. H. Crabtree, *J. Am. Chem. Soc.* **2013**, *135*, 10837–10851.
[33] K. R. Yang, A. J. Matula, G. Kwon, J. Hong, W. Sheehan, J. M. Thomsen, G. W. Brudvig, R. H. Crabtree, D. M. Tiede, L. X. Chen, V. S. Batista, *J. Am. Chem. Soc.* **2016**, *138*, 5511–5514.
[34] A. Bucci, A. Savini, L. Rocchigiani, C. Zuccaccia, S. Rizzato, A. Albinati, A. Llobet, A. Macchioni, *Organometallics* **2012**, *31*, 8071–8074.
[35] U. Hintermair, S. M. Hashmi, M. Elimelech, R. H. Crabtree, *J. Am. Chem. Soc.* **2012**, *134*, 9785–9795.

[36] J. M. Thomsen, S. W. Sheehan, S. M. Hashmi, J. Campos, U. Hintermair, R. H. Crabtree, G. W. Brudvig, *J. Am. Chem. Soc.* **2014**, *136*, 13826–13834.
[37] G. Menendez Rodriguez, A. Bucci, R. Hutchinson, G. Bellachioma, C. Zuccaccia, S. Giovagnoli, H. Idriss, A. Macchioni, *ACS Energy Lett.* **2017**, *2*, 105–110.
[38] A. R. Parent, R. H. Crabtree, G. W. Brudvig, *Chem. Soc. Rev.* **2013**, *42*, 2247–52.
[39] I. Corbucci, A. Petronilho, H. Müller-Bunz, L. Rocchigiani, M. Albrecht, A. Macchioni, *ACS Catal.* **2015**, *5*, 2714–2718.
[40] M. Navarro, M. Li, H. Müller-Bunz, S. Bernhard, M. Albrecht, *Chem. Eur. J.* **2016**, *22*, 6740–6745.
[41] A. Bucci, G. M. Rodriguez, G. Bellachioma, C. Zuccaccia, A. Poater, L. Cavallo, A. Macchioni, *ACS Catal.* **2016**, *6*, 4559–4563.
[42] Z. Codolà, L. Gómez, S. T. Kleespies, L. Que, M. Costas, J. Lloret-Fillol, *Nat. Commun.* **2015**, *6*, 5865.
[43] O. Diaz-Morales, T. J. P. Hersbach, D. G. H. Hetterscheid, J. N. H. Reek, M. T. M. Koper, *J. Am. Chem. Soc.* **2014**, *136*, 10432–10439.
[44] D. Bourissou, O. Guerret, F. P. Gabbaï, G. Bertrand, *Chem. Rev.* **2000**, *100*, 39–92.
[45] F. E. Hahn, M. C. Jahnke, *Angew. Chem. Int. Ed.* **2008**, *47*, 3122–3172; *Angew. Chem.* **2008**, *120*, 3166.
[46] M. Melaimi, M. Soleilhavoup, G. Bertrand, *Angew. Chem. Int. Ed.* **2010**, *49*, 8810–8849; *Angew. Chem.* **2010**, *122*, 8992.
[47] O. Schuster, L. Yang, H. G. Raubenheimer, M. Albrecht, *Chem. Rev.* **2009**, *109*, 3445–3478.
[48] R. Pokhrel, M. K. Goetz, S. E. Shaner, X. Wu, S. S. Stahl, *J. Am. Chem. Soc.* **2015**, *137*, 8384–8387.
[49] E. V. Sackville, F. Marken, U. Hintermair, *ChemCatChem* **2018**, *10*, 4280–4291.
[50] H. C. Kolb, M. G. Finn, K. B. Sharpless, *Angew. Chem. Int. Ed.* **2001**, *40*, 2004–2021; *Angew. Chem.* **2001**, *113*, 2056.
[51] J. E. Moses, A. D. Moorhouse, *Chem. Soc. Rev.* **2007**, *36*, 1249–1262.
[52] M. Meldal, C. W. Tomoe, *Chem. Rev.* **2008**, *108*, 2952–3015.
[53] P. Mathew, A. Neels, M. Albrecht, *J. Am. Chem. Soc.* **2008**, *130*, 13534–13535.
[54] G. Guisado-Barrios, J. Bouffard, B. Donnadieu, G. Bertrand, *Angew. Chem. Int. Ed.* **2010**, *49*, 4759–4762; *Angew. Chem.* **2010**, *122*, 4869.
[55] K. F. Donnelly, A. Petronilho, M. Albrecht, *Chem. Commun.* **2013**, *49*, 1145–1159.
[56] B. Schulze, U. S. Schubert, *Chem. Soc. Rev.* **2014**, *43*, 2522–71.
[57] D. Schweinfurth, L. Hettmanczyk, L. Suntrup, B. Sarkar, *Z. Anorg. Allg. Chem.* **2017**, *643*, 554–584.
[58] Á. Vivancos, C. Segarra, M. Albrecht, *Chem. Rev.* **2018**, *118*, 9493–9586.
[59] M. H. V. Huynh, T. J. Meyer, *Chem. Rev.* **2007**, *107*, 5004–5064.
[60] J. Depasquale, M. Kumar, M. Zeller, E. T. Papish, *Organometallics* **2013**, *32*, 966–979.
[61] D. Hong, M. Murakami, Y. Yamada, S. Fukuzumi, *Energy Environ. Sci.* **2012**, *5*, 5708–5716.
[62] M. Navarro, C. A. Smith, M. Li, S. Bernhard, M. Albrecht, *Chem. Eur. J.* **2018**, *24*, 6386–6398.
[63] J. Huang, J. T. Hong, S. H. Hong, *Eur. J. Org. Chem.* **2012**, 6630–6635.
[64] J. Depasquale, I. Nieto, L. E. Reuther, C. J. Herbst-Gervasoni, J. J. Paul, V. Mochalin, M. Zeller, C. M. Thomas, A. W. Addison, E. T. Papish, *Inorg. Chem.* **2013**, *52*, 9175–9183.
[65] D. Tapu, D. A. Dixon, C. Roe, *Chem. Rev.* **2009**, *109*, 3385–3407.
[66] H. V. Huynh, *Chem. Rev.* **2018**, *118*, 9457–9492.
[67] C. Hansch, A. Leo, R. W. Taft, *Chem. Rev.* **1991**, *91*, 165–195.
[68] a) R. Maity, S. Hohloch, C. Y. Su, M. van der Meer, B. Sarkar, *Chem. Eur. J.* **2014**, *20*, 9952–9961; b) A. Ruff, C. Kirby, B. C. Chan, A. R. O'Connor, *Organometallics* **2016**, *35*, 327–335.
[69] A. Petronilho, J. A. Woods, H. Mueller-Bunz, S. Bernhard, M. Albrecht, *Chem. Eur. J.* **2014**, *20*, 15775–15784.
[70] Notably, a related complex of the same ligand with ruthenium(II) does not show any ligand bond distortion, thus supporting the model that packing rather than intrinsic ligand effects lead to the unusual bond lengths observed in iridium complex **10**.
[71] R. Lalrempuia, N. D. McDaniel, H. Müller-Bunz, S. Bernhard, M. Albrecht, *Angew. Chem. Int. Ed.* **2010**, *49*, 9765–9768; *Angew. Chem.* **2010**, *122*, 9959.
[72] M. D. Levi, G. Salitra, N. Levy, D. Aurbach, J. Maier, *Nat. Mater.* **2009**, *8*, 872–875.
[73] M. D. Levi, N. Levy, S. Sigalov, G. Salitra, D. Aurbach, J. Maier, *J. Am. Chem. Soc.* **2010**, *132*, 13220–13222.
[74] M. D. Levi, S. Sigalov, D. Aurbach, L. Daikhin, *J. Phys. Chem. C* **2013**, *117*, 14876–14889.
[75] D. G. H. Hetterscheid, *Chem. Commun.* **2017**, *53*, 10622–10631.
[76] A. H. Wonders, T. H. M. Housmans, V. Rosca, M. T. M. Koper, *J. Appl. Electrochem.* **2006**, *36*, 1215–1221.
[77] K. G. Kottrup, D. G. H. Hetterscheid, *Chem. Commun.* **2016**, *52*, 2643–2646.
[78] It is important to note that the actual trace of gaseous products observed between different experiments cannot be compared directly. The actual amount of gas that is taken up by the OLEMS depends on the distance in which the OLEMS tip is positioned with respect to the electrode. This is not constant and cannot be calibrated neither. The quantitative comparison was performed on basis of the current density, taking into account that the trace of the gaseous products perfectly follows the profile of the current.
[79] S. W. Sheehan, J. M. Thomsen, U. Hintermair, R. H. Crabtree, G. W. Brudvig, C. A. Schmuttenmaer, *Nat. Commun.* **2015**, *6*, 6469.
[80] D. G. H. Hetterscheid, C. J. M. van der Ham, O. Diaz-Morales, M. W. G. M. Verhoeven, A. Longo, D. Banerjee, J. W. Niemantsverdriet, J. N. H. Reek, M. C. Feiters, *Phys. Chem. Chem. Phys.* **2016**, *18*, 10931–10940.
[81] J. F. Moulder, J. Chastain, R. C. King, *Handbook of X-ray Photoelectron Spectroscopy: A Reference Book of Standard Spectra for Identification and Interpretation of XPS Data*, Physical Electronics Division (Perkin-Elmer Corp.), Eden Prairie, Minnesota, **1995**.
[82] P. Abril, M. P. Del Río, C. Tejel, T. W. G. M. Verhoeven, J. W. H. Niemantsverdriet, C. J. M. van der Ham, K. G. Kottrup, D. G. H. Hetterscheid, *ACS Catal.* **2016**, *6*, 7872–7875.
[83] I. Stengel, A. Mishra, N. Pootrakulchote, S. J. Moon, S. M. Zakeeruddin, M. Grätzel, P. Bäuerle, *J. Mater. Chem.* **2011**, *21*, 3726–3734.
[84] J. M. Keith, *J. Org. Chem.* **2010**, *75*, 2722–2725.
[85] B. Chattopadhyay, C. I. Rivera Vera, S. Chuprakov, V. Gevorgyan, *Org. Lett.* **2010**, *12*, 2166–2169.
[86] S. Sabater, H. Müller-Bunz, M. Albrecht, *Organometallics* **2016**, *35*, 2256–2266.
[87] R. G. Ball, W. A. G. Graham, D. M. Heinekey, J. K. Hoyano, A. D. McMaster, B. M. Mattson, S. T. Michel, *Inorg. Chem.* **1990**, *29*, 2023–2025.
[88] C. J. M. van der Ham, F. Isik, T. W. G. M. Verhoeven, J. W. Niemantsverdriet, H. D. G. H, *Catal. Today* **2017**, *290*, 33–38.
[89] *CrysAlisPro (Version 1.171.34.44)*. Oxford Diffraction Ltd., Yarnton, Oxfordshire, UK, **2010**.
[90] P. Macchi, H. B. Bürgi, A. S. Chimpri, J. Hauser, Z. Gál, *J. Appl. Crystallogr.* **2011**, *44*, 763–771.
[91] G. M. Sheldrick, *Acta Crystallogr., Sect. A* **2015**, *71*, 3–8.
[92] G. M. Sheldrick, *Acta Crystallogr., Sect. C* **2015**, *71*, 3–8.

Received: January 29, 2020